nature structural & molecular biology

ARTICLES

https://doi.org/10.1038/s41594-019-0248-4

Cryo-EM structures of four polymorphic TDP-43 amyloid cores

Qin Cao[1,3], David R. Boyer[1,3], Michael R. Sawaya[1], Peng Ge[2] and David S. Eisenberg[1*]

The DNA and RNA processing protein TDP-43 undergoes both functional and pathogenic aggregation. Functional TDP-43 aggregates form reversible, transient species such as nuclear bodies, stress granules, and myo-granules. Pathogenic, irreversible TDP-43 aggregates form in amyotrophic lateral sclerosis and other neurodegenerative conditions. Here we find the features of TDP-43 fibrils that confer both reversibility and irreversibility by determining structures of two segments reported to be the pathogenic cores of human TDP-43 aggregation: SegA (residues 311–360), which forms three polymorphs, all with dagger-shaped folds; and SegB A315E (residues 286–331 containing the amyotrophic lateral sclerosis hereditary mutation A315E), which forms R-shaped folds. Energetic analysis suggests that the dagger-shaped polymorphs represent irreversible fibril structures, whereas the SegB polymorph may participate in both reversible and irreversible fibrils. Our structures reveal the polymorphic nature of TDP-43 and suggest how the A315E mutation converts the R-shaped polymorph to an irreversible form that enhances pathology.

Amyloid-forming proteins seem to violate the central tenant of protein science—that amino acid sequence determines structure and function[1]. In contrast with globular and membrane proteins, each of which fold into a single functional structure, a given amyloid-forming sequence can fold into several distinct polymorphic structures[2,3].

Irreversible, hyperphosphorylated, amyloid-like aggregates of C-terminal segments of TDP-43 are the primary pathology of ALS and frontotemporal lobar degeneration with TDP-43 inclusions (FTLD-TDP)[4–6]. These aggregates have also been found in Alzheimer's, Parkinson's, CTE, Huntington's disease, limbic-predominant age-related TDP-43 encephalopathy (LATE) and inclusion body myopathies, among others[7–11]. Because TDP-43 functions in several essential steps of RNA metabolism[12,13], it is widely considered that TDP-43 aggregation is toxic through a loss-of-function mechanism[14–16]. Structural studies of amyloid fibrils of β-amyloid[17,18], tau[19,20], α-synuclein[2], and β2-microglobulin[21] have revealed polymorphs and insight into pathogenesis. Here, we use cryo-EM to determine the overall folds of TDP-43 amyloid cores, expanding structural information about both reversible and irreversible aggregation beyond the local interactions previously revealed by crystallography[22,23].

Results

Generating TDP-43 fibrils. We screened for TDP-43 fibrils by incubating various SUMO-tagged TDP-43 segments in a test tube after cleavage of the SUMO-tag (Supplementary Fig. 1a and Supplementary Table 1). We first aimed to produce fibrils formed by full-length TDP-43, a pathogenic C-terminal fragment (CTF, 208–414) truncation product that is enriched in diseased brain[24], or by the low-complexity domain (LCD, 274–414) which is considered to be necessary for TDP-43 aggregation[22,25,26]. However, despite our efforts at optimization, we observed only highly clumped fibril-like structures and disordered aggregates that were not suitable for cryo-EM structure determination (Supplementary Fig. 1b). We suspect that this may be due to the ability of longer constructs of TDP-43 to participate in multivalent interactions, possibly through LARKS[22,27] or other adhesive segments outside the LCD[23]. These multivalent interactions have been shown to assemble networks of protein chains and could explain why longer segments of TDP-43 form amorphous aggregates or fibril clumps. This observation is in line with the role of TDP-43 in phase separation and stress granule formation, which requires the presence of multivalent interactions[27].

To overcome the hurdle of the disordered assembly of longer segments of TDP-43, we implemented a 'divide and conquer' approach, whereby we selected known aggregation cores for structure determination. We chose SegA (residues 311–360) and SegB (residues 286–331), guided by the following evidence. SegA was previously identified as an aggregation core of TDP-43 because its deletion decreases TDP-43 aggregation in vitro and in cells, whereas addition of SegA to the aggregation-resistant *Caenorhabditis elegans* TDP-43 homolog induces aggregation[28]. Fibrils of SegB are toxic to primary neurons, and the ALS hereditary mutation A315T together with phosphorylation of the threonine, which is speculated to occur in hyperphosphorylated aggregates of TDP-43 in disease, increases cytotoxicity of SegB[29]. With these findings in mind, we selected SegB A315E, another hereditary mutation with similar effects to those of A315T[29–32] and a mimic of A315T with phosphorylation, in order to visualize the structure of a second possible TDP-43 aggregation core and to gain insight into the molecular mechanism of mutation-enhanced TDP-43 pathology. The importance of SegA and SegB in full-length TDP-43 aggregation is also supported by other studies finding that amyloid fibrils containing either a core region of SegA (residues 314–353) or a region similar to SegB (residues 274–313) can template aggregation of full-length TDP-43 in SH-SY5Y human neuronal cells[33]. Likewise, in the same cell line, deletion of these two regions (residues 314–353 or 274–313) from full-length TDP-43 inhibits aggregation.

Architecture of SegA and SegB fibrils. As we expected, fibrils formed by SegA and SegB A315E were more homogenous and

[1]Department of Chemistry and Biochemistry and Biological Chemistry, UCLA-DOE Institute, Molecular Biology Institute, and Howard Hughes Medical Institute, UCLA, Los Angeles, CA, USA. [2]California NanoSystem Institute, UCLA, Los Angeles, CA, USA. [3]These authors contributed equally: Qin Cao, David R. Boyer. *e-mail: david@mbi.ucla.edu

less bundled than longer segments of TDP-43, including SegAB (286–360), containing aggregation cores of both SegA and SegB (Supplementary Fig. 1b). This observation supports the idea that eliminating competing multivalent interactions helps to produce homogenous fibrils of isolated amyloid cores. Using these homogenous preparations, we determined three polymorphic fibril structures of SegA (termed SegA-sym, SegA-asym and SegA-slow) and one of SegB A315E (Fig. 1, Supplementary Figs. 2–4 and Table 1; technical details in Methods).

All four fibrils are formed from gradually twisting β-sheets that run the entire length of the fibrils (Fig. 1b–e). A thin slab or 'layer' perpendicular to each fibril axis (Fig. 1) shows that individual SegA and SegB chains are each confined within an essentially two-dimensional layer, in contrast with globular and membrane proteins, whose folds occupy three dimensions. Identical layers stack on one another, creating β-sheets that are parallel and in register. Each layer contains two or more protein chains, giving rise to a corresponding number of protofilaments in the fibril.

The dagger-shaped fold in SegA polymorphs. SegA polymorphs all share a dagger-shaped fold comprised of residues 312–346, with the hydrophobic residues from Phe313 to Ala341 forming tight hydrophobic interactions and a sharp 160° kink at Gln327, forming the dagger tip (Fig. 2a–d and Supplementary Fig. 5; detailed comparison below and Supplementary Figs. 5 and 6). The three SegA polymorphs mainly differ in the number of protofilaments and symmetry. SegA-sym fibrils contain two protofilaments related by a pseudo-2_1 axis, whereas SegA-asym contains two protofilaments with somewhat different conformations. SegA-slow fibrils contain four protofilaments: two protofilaments related by a central two-fold axis, containing 50 ordered residues, flanked by two other protofilaments containing only ten ordered residues.

The core region of the dagger-shaped fold (residues 320–334) is almost identical in all four dagger-shaped folds of the three SegA polymorphs (Fig. 2a and Supplementary Fig. 5). Detailed single chain superposition showed that SegA-sym and the long chain of SegA-asym have nearly identical dagger-shaped folds, with the 'stem' of the long chain SegA-asym (Ala341 to Ser347) bent approximately 40° (Fig. 2c). This bending of the long chain SegA-asym stem forces a 40° bend in the 'blade' of the SegA-asym short chain relative to the reference SegA-sym fold, corresponding to the shift in registration of the stem hydrophobic interdigitation (Supplementary Fig. 5). Additionally, the 'stem' of SegA-slow (Ala341 to Ser347) is bent approximately 50° compared with that of SegA-sym (Supplementary Fig. 5), causing a significant conformational change at Met336. Furthermore, the interaction of the termini in SegA-slow causes a conformational change at Phe313, Phe316 and Met339 and sequesters Met311 away from the solvent, burying it in the hydrophobic core (Supplementary Fig. 5).

The protofilament interface in SegA-sym and SegA-asym are similar (Supplementary Fig. 6a,b), with slight differences in the region that has a 40° bend (Supplementary Fig. 6b). We named this region the continuous interface, because it is formed by two continuous chains; the broken interface in SegA-slow is formed by the interaction of the termini (Supplementary Fig. 5). The continuous interface has a hydrophobic core formed by Met336 and Leu340 from both monomers and a hydrogen bond network toward the edges (Fig. 2d and Supplementary Fig. 6a). The broken interface is formed mainly by the tight packing of Met359 and the hydrogen bond network of the peripheral asparagine residues (Supplementary Fig. 6a). We observed only part of the continuous interface in SegA-slow, probably owing to the conformational change of Met336 (Supplementary Fig. 6c,d; detailed model building in Methods).

We note that SegA-sym and SegA-asym structures are compatible with full-length TDP-43 because of their free N and C termini. The SegA-slow structure is an artifact of the truncation, because the N and C termini are sequestered in the center of the fibrils (Fig. 1d and Supplementary Fig. 6a). Therefore, in this analysis, we mostly focused on SegA-sym and SegA-asym. However, we note that the SegA-slow structure provides valuable information. First, the SegA-slow structure contains the dagger-shaped fold, demonstrating conservation of the fold in the three polymorphs we observed for SegA (Supplementary Fig. 5). The incompatibility of SegA-slow with full-length TDP-43 comes from the tail region (residues 347–360), which is external to the dagger-shaped fold (Supplementary Fig. 7a). Thus, taken alone, the dagger-shaped fold in SegA-slow (residues 312–346) is still compatible with full-length TDP-43, as in SegA-sym and SegA-asym. Second, the tail region hairpin structure (residues 342–360) in SegA-slow is also compatible with full-length TDP-43 when separated from the dagger-shaped fold, with free N and C termini (Supplementary Fig. 7a). This hairpin structure is formed by tightly packed hydrophilic zippers stabilized by extensive hydrogen bonds (Supplementary Fig. 7b). On the basis of the above analysis, we speculate that this hairpin structure may also be involved in TDP-43 aggregation as another segmental polymorph. Further study is needed to test this hypothesis and to identify if this hairpin contributes to reversible or irreversible aggregation of TDP-43. Third, our SegA-slow structure provides, to our knowledge, the first atomic evidence in support of secondary seeding of amyloid fibrils. Secondary seeding is considered to occur when the side of preformed fibrils serves as a template for new monomers to nucleate into an amyloid fibril. This process is in contrast to primary seeding, in which molecules are added to the top or bottom of preformed fibrils. In this case, the extra density near Gln331 and Met323 of the long chain of SegA-slow indicates that secondary seeding can occur on these regions (Fig. 1d). Because the long chain of SegA-slow contains all 50 residues in SegA, the extra density must come from other SegA molecules, thus supporting a secondary seeding mechanism. In comparison, similar extra density has been observed in other amyloid fibril structures, such as the tau paired helical filament (PHF)[19], but in these structures, the ordered fibril core does not contain all residues of the molecule. Therefore, it is unclear whether these densities come from binding of a different molecule or from sequences outside of the fibril core of the same molecule.

The R-shaped fold in the SegB fibril. SegB A315E forms fibrils of a single morphology, in contrast with polymorphic SegA. These fibrils are characterized by an R-shaped fold spanning residues 288–319 (Fig. 2e,f). Overall, the R-shaped fold is more highly kinked than the dagger-shaped fold (Fig. 1b–e), probably owing to the abundance of glycine residues. Each fibril is wound from four protofilaments (Fig. 2e). The two inner protofilaments are related through a tight, pseudo-2_1 symmetric interface (Fig. 2e,g). These protofilaments are flanked by two outer protofilaments through an asymmetric interface (Fig. 2e,g). The symmetric interfaces are formed by small side chain residues (Gly298 and Gly300) in the middle (reminiscent of the homodimer interface in the tau PHF structure from Alzheimer's disease[19]) and hydrogen bonds among Gln303, Gly295, Ala297 and Gln301 (Fig. 2g and Supplementary Fig. 8a). The asymmetric interfaces are formed by hydrophobic interaction of Ile318, Phe316 with Phe289, insertion of Leu299 into the pocket formed by the main chain of Asn306–Gly309, hydrophobic interaction of Phe289 (from another inner chain) and the main chain Asn303–Gly304, and hydrogen bonds among Met311, Asn312 and Gly290–Ser292 (Fig. 2g, right and Supplementary Fig. 8a).

The overall R-shaped folds of the inner and outer chain of the SegB A315E fibril are similar but with some salient differences (Fig. 2f), which recall the positional polymorphism observed in a different, shorter TDP-43 segment[23]. The head region of the inner chain is formed by the hydrophobic interaction of Leu299, Met307, Met311 and Phe313, as well as by Asn302 and Ser305 hydrogen bonding; in the outer chain, Leu299 is flipped outside the head to

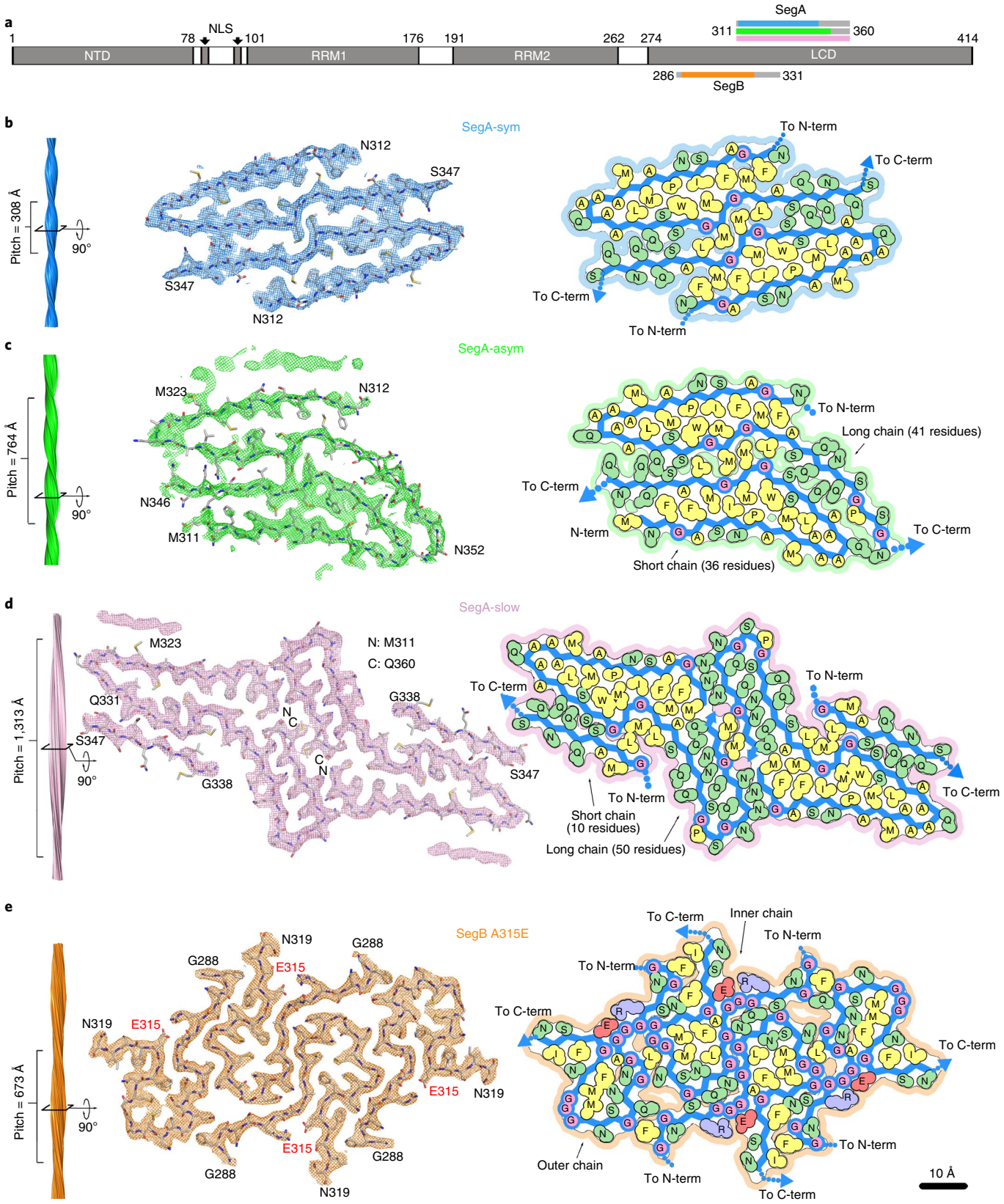

Fig. 1 | Cryo-EM structures of TDP-43 polymorphic fibrils. a, Schematic of full-length TDP-43. SegA (residues 311–360) and SegB (residues 286–331) identified for structural determination are shown as gray bars, above and below the LCD, respectively. The colored bars show the range of residues visualized in the structure of each polymorph. **b**–**e**, Left: fibril reconstructions showing left-handed twist and pitch; middle: density and atomic model of one cross-sectional layer of each fibril; right: schematic model showing protein chain (blue) and residues (hydrophobic in yellow, polar in green, glycine in pink, glutamate in red and arginine in blue). N-term, N terminus; C-term, C terminus.

Table 1 | Cryo-EM Data collection, refinement and validation statistics

	SegA-sym (EMD-9339, PDB 6N37)	SegA-asym (EMD-9350, PDB 6N3B)	SegA-slow (EMD-9349, PDB 6N3A)	SegB A315E (EMD-0334, PDB 6N3C)
Data collection and processing				
Magnification	×130,000	×130,000	×130,000	×130,000
Voltage (kV)	300	300	300	300
Electron exposure (e^-/Å^2)	44	44	44	44
Defocus range (μm)	1.1–3.9	1.1–4.4	1.0–9.9	0.5–4.9
Pixel size (Å)	1.064	1.064	1.064	1.060
Symmetry imposed	C_1	C_1	C_2	C_1
Helical rise (Å)	2.38	4.81	4.84	2.41
Helical twist (°)	178.61	−2.27	179.34	179.36
Initial particle images (no.)	92,568	92,568	499,065	361,182
Final particle images (no.)	8,033	15,464	167,087	44,085
Map resolution (Å)	3.8	3.8	3.3	3.3
FSC threshold	0.5	0.5	0.143	0.143
Map resolution range (Å)	200–3.8	200–3.8	200–3.3	200–3.3
Refinement				
Initial model used	De novo	De novo	De novo	De novo
Model resolution (Å)	3.8	3.8	3.2	3.2
FSC threshold	0.5	0.5	0.5	0.5
Model resolution range (Å)	200–3.8	200–3.8	200–3.2	200–3.2
Map sharpening *B* factor (Å^2)	−87	−93	−134	−154
Model composition				
Nonhydrogen atoms	2,580	2,735	4,310	4,260
Protein residues	360	385	600	640
B factors (Å^2)				
Protein	75.8	105.4	108.6	72.2
R.m.s. deviations				
Bond lengths (Å)	0.009	0.010	0.008	0.009
Bond angles (°)	1.548	1.372	1.143	1.306
Validation				
MolProbity score	2.28	2.47	2.25	2.35
Clashscore	12.95	22.11	17.25	18.47
Ramachandran plot				
Favored (%)	85.3	86.3	91.1	88.5
Allowed (%)	14.7	13.7	8.9	11.5

mediate the heterodimer interaction between the inner and outer chain (Fig. 2f). Consequently, the head region of the outer chain is formed by the hydrophobic interaction of Met307, Met311 and Phe313, together with hydrogen bonds formed by Asn301, Asn302 and Ser305 (Fig. 2f and Supplementary Fig. 8b). The neck region of both chains is formed by hydrophobic interaction between Ala297 and Phe313 and the Arg293–Glu315 salt bridge. The 70° bend of the Phe316–Asn319 leg of the outer chain relative to the inner chain is probably caused by the heterodimer interface formed by the legs of the inner and outer chain that restricts the conformation of the inner chain.

In all four R folds, we observed a salt bridge between Arg293 and Glu315, enabled by the pathogenic A315E mutation. The Arg293–Glu315 salt bridge is not formed by the residues from the same layer along the fibril axis. Rather, each Arg293 interacts with the Glu315 from one or two layers above (Fig. 2h), which may affect the kinetics of fibril growth and nucleation. This salt bridge suggests a mechanistic explanation for the inclination of A315E toward TDP-43 pathology (Discussion). Model building suggests that wild-type SegB can form the same R-shaped fold as A315E, with Ala315 participating in a hydrophobic interaction with Ala297 and Phe313. This hypothesis is supported by the similar stability and morphology of wild-type SegB fibrils compared with SegB A315E fibrils in our thermostability assays (Supplementary Fig. 1c) and by the cross-seeding ability of SegB and SegB A315E (Supplementary Fig. 1e).

Notably, although TDP-43 can form either the dagger-shaped polymorph of SegA or the R-shaped polymorph of SegB, it is unlikely that a given molecule of TDP-43 can form both polymorphs simultaneously. This exclusivity is indicated in a superposition of the two folds in the overlapping segment Asn312–Asn319 (Supplementary Fig. 8c). The superposition reveals that steric overlap between the main chains of SegA and SegB would occur if both folds were formed by a single TDP-43 molecule containing both SegA and SegB sequences.

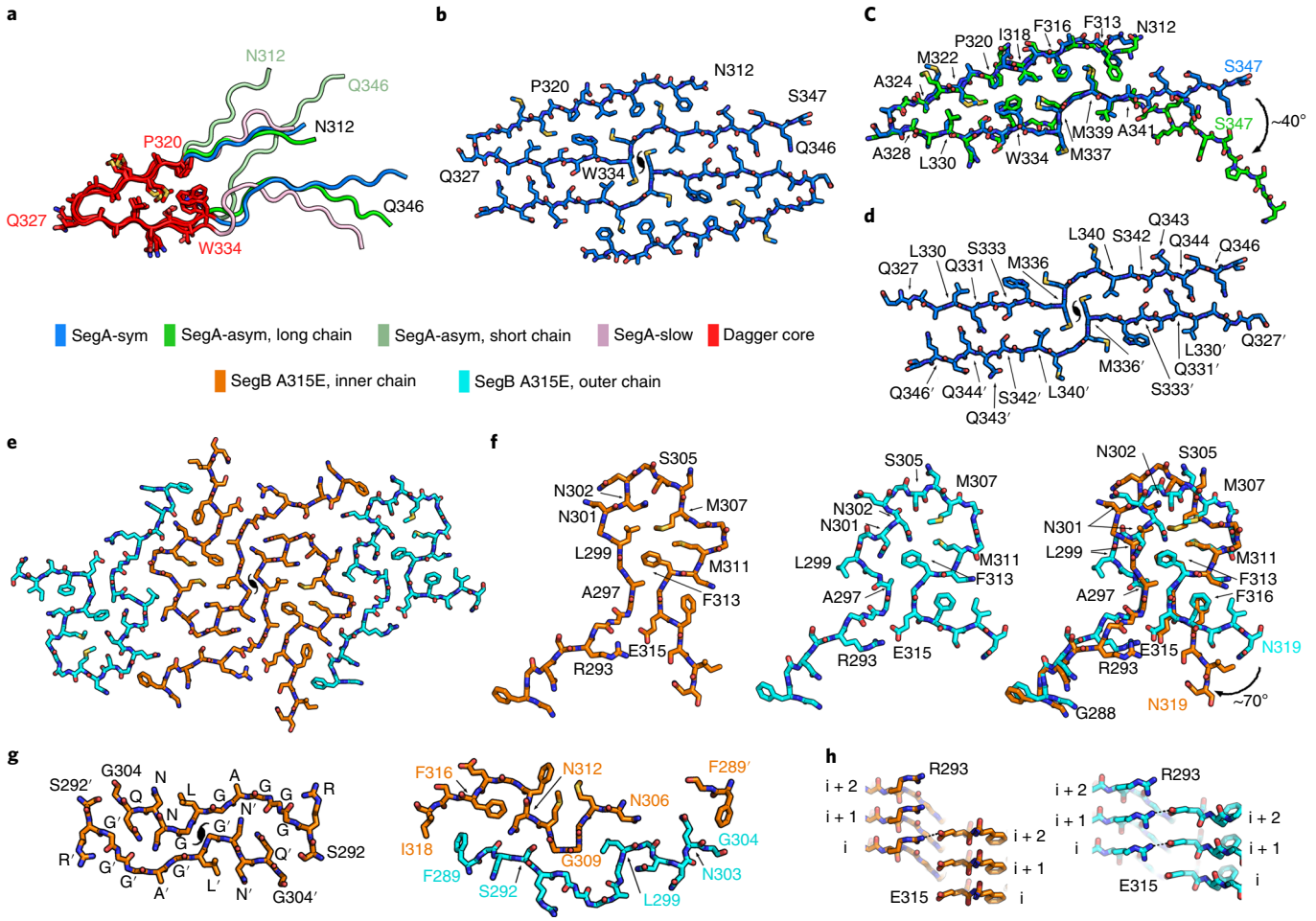

Fig. 2 | Structure of the dagger-shaped fold and the R-shaped fold. a, Superposition of the dagger-shaped folds (residues 312–346) in three SegA polymorphic fibrils. The core region of the dagger-shaped folds (residues 320–334) is in red with side chains shown, and the rest of the dagger-shaped fold is colored according to the key. **b**, Atomic model of SegA-sym. **c**, Pairwise superposition of the dagger-shaped fold of SegA-sym versus the SegA-asym long chain. **d**, Continuous dimer interface of SegA-sym. **e**, Atomic model of SegB A315E. Each of the four chains is R shaped, with a pseudo-2_1 axis relating the two pairs. The inner two chains are identical, as are the two outer chains. **f**, Structures of the inner (left) and outer (middle) chains and their superposition (right). Notice the proximity of R293 (Arg293) to the pathogenic variant E315 (Glu315), which replaces A315 (Ala315) in the reference sequence. **g**, View parallel to the fibril axis showing the symmetric interface between the two inner chains (left) and the asymmetric interface between the inner and outer chains (right). **h**, View perpendicular to the fibril showing the interlayer interaction of R293 (Arg293) with E315 (Glu315) on the inner chain (left) and outer chain (right). Detailed alignment parameters and r.m.s.d. values are listed in Supplementary Table 2.

Stability of SegA and SegB fibrils. The extensive hydrophobic interactions and hydrogen bonds observed in both the dagger- and R-shaped folds suggest that both SegA and SegB A315E fibrils are irreversible. To examine this hypothesis, we calculated modified atomic solvation energies (Methods) to quantify the stabilities of the fibrils. The calculated stabilities of both the dagger- and R-shaped fold fibrils (represented by energy per layer and per residue) were comparable to those of other pathogenic amyloid fibrils, such as the Alzheimer's and Pick's disease fibrils (Fig. 3 and Table 2). In contrast, the stability of fused in sarcoma (FUS) fibrils, thought to be reversible[34], was distinctly lower.

We performed thermostability assays to validate our energetic calculations. When heated to 75 °C for 30 min, fibrils formed by SegA, SegB, and SegB A315E were all stable, whereas fibrils formed by mCherry-FUS-LCD (composed of residues 1–214, identical to the sequence determined in the FUS ssNMR structure but with a His-tag replacing mCherry[34]) disappeared upon heating at 60 °C (Supplementary Fig. 1c). These results are consistent with our energetic calculations and support the idea that the dagger- and R-shaped fold fibrils are irreversible.

SegA and SegB folds can be adopted by longer TDP-43 segments. Several lines of evidence suggest that the dagger- and R-shaped folds can be adopted by longer TDP-43 segments such as the pathogenic TDP-CTF fragment. (1) Structural conservation: the core region (residue 320–334) of the dagger-shaped fold is structurally conserved in all four dagger-shaped folds despite differences in local environment (Fig. 2a). This high degree of structural conservation suggests that this core region of the dagger-shaped fold is thermodynamically stable, kinetically accessible and likely to be present in other polymorphs (perhaps including disease-relevant TDP-43 aggregates). (2) Model building: the outward facing disposition of the termini in these folds allows longer TDP-43 structures to be modeled from these cores without steric interference. (3) Cross-seeding: fibrils formed by TDP-CTF can seed SegA and SegB A315E monomer (Supplementary Fig. 1f), and SegA and SegB A315E fibrils can seed TDP-LCD monomer (Fig. 4b) (owing to its rapid aggregation, TDP-CTF monomer could not be used to measure seeding, and we instead used TDP-LCD monomer, as the LCD is required for TDP-43 aggregation[22,25,26]). (4) Mutagenesis experiments with TDP-CTF reported previously[22] and described below.

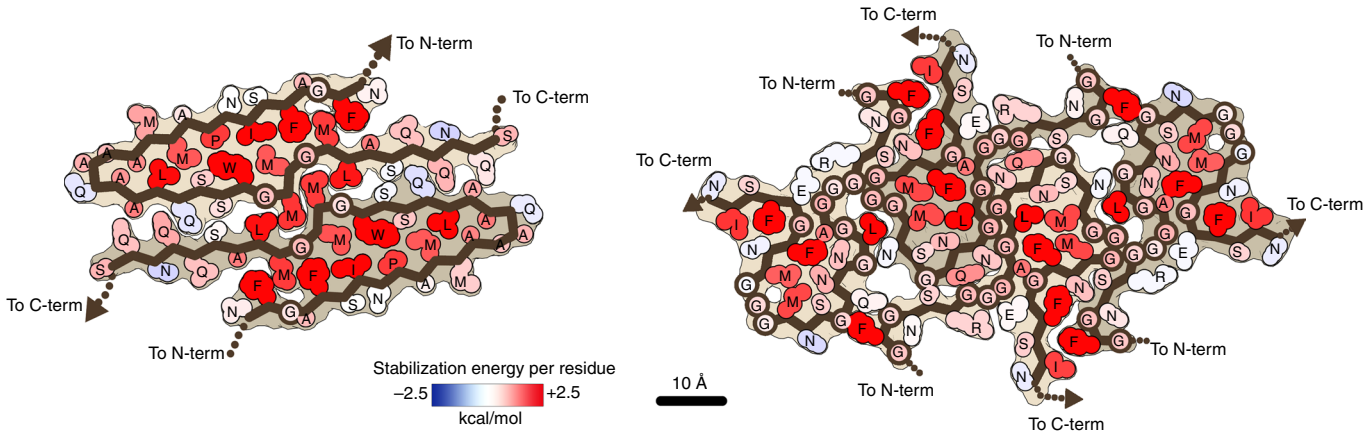

Fig. 3 | Calculated solvation energy maps for TDP-43 fibrils based on atomic solvation parameters. Solvation energy maps of SegA-sym (left) and SegB A315E (right). Residues are colored from unfavorable (blue, −2.5 kcal/mol) to favorable stabilization energy (red, 2.5 kcal/mol). Notice that both the dagger-shaped fold (SegA-sym) and the R-shaped fold (SegB A315E) show stable cores.

Table 2 | Comparative solvation energy calculations

Fibril structure	Energy per layer (kcal/mol)	Energy per residue (kcal/mol)
SegA-sym (PDB 6N37)	73	1.0
SegA-asym (PDB 6N3B)	76	0.97 (long chain, 0.92; short chain, 1.04)
SegB A315E (PDB 6N3C)	110	0.86 (inner chain, 0.94; outer chain, 0.79)
Tau PHF (PDB 5O3L)	128	0.88
Tau SF (PDB 5O3T)	144	1.0 (chain A, 0.98; chain B, 1.02)
Tau Pick's (PDB 6GX5)	98	1.0
FUS (PDB 5W3N)	41	0.66

We found that five individual point mutations to tryptophan delayed aggregation of TDP-CTF; these sterically conflict with the tightly packed dagger-shaped (A324W, L330W, Q331W, M337W) and R-shaped folds (Q303W) and delay aggregation of TDP-CTF[22]. In SegA-sym, three of these mutation sites (Ala324, Leu330 and Met337) point toward the center of the dagger-shaped fold, and the other (Gln331) points toward the 'continuous dimer interface' (Fig. 2b and Supplementary Fig. 9a,b), and in SegB A315E, Gln303 of the inner chain is buried within the interchain interface (Supplementary Fig. 9a,b and Supplementary Fig. 10). All four sites are buried in a tightly packed interface that cannot tolerate a tryptophan replacement. Similarly, the mutations A324E and M337E, which are disruptive to the dagger-shaped fold, inhibit aggregation of full-length TDP-43 in cells[28]. As negative controls, we found that A326W and G304W—located in a solvent-exposed environment of the dagger-shaped fold and a loose cavity of the R-shaped fold, respectively—can tolerate the bulky tryptophan and did not delay aggregation of TDP-CTF (Supplementary Fig. 1d and Supplementary Fig. 9a,b)[22]. Furthermore, a key stabilizing feature of SegB A315E, the Arg293–Glu315 salt bridge, is similarly important for TDP-CTF aggregation. We designed two double mutants, R293E A315E and R293E A315R, based on our structure of SegB A315E. R293E A315E disrupted the R-shaped fold by electrostatic repulsion, whereas R293E A315R favored the R-shaped fold by restoring the salt bridge. In accordance with our model, R293E A315E reduced TDP-CTF aggregation, whereas R293E A315R enhanced TDP-CTF aggregation (Supplementary Fig. 1d).

These results suggest that both the dagger- and the R-shaped folds are accessible to TDP-CTF molecules so that disrupting either one blocks one pathway to fibril formation and thus delays aggregation of TDP-CTF. The observation that none of these mutations targeting the dagger- or R-shaped fold fully eliminates aggregation supports our hypothesis that TDP-CTF can form fibrils using one of multiple aggregation cores, including the dagger- or R-shaped fold, or possibly others not yet discovered. In short, conservation of the dagger fold, modeling, seeding experiments, and mutational analysis all suggest that TDP-CTF can form the folds we observed.

Relevance of the dagger and R folds in human disease. We investigated whether the dagger- and R-shaped folds are relevant to TDP-43 fibrils in human disease, motivated by the irreversibility of fibrils formed by these folds and the likely accessibility to both folds of TDP-CTF. The scarcity of TDP-43 fibrils in autopsied brains of patients with ALS or FTLD daunts structure determination of patient-derived TDP-43 fibrils, so we used seeding experiments to examine the possibility that our structures represent folds adopted by TDP-43 in disease.

We seeded both SegA and SegB A315E monomer with sarkosyl-insoluble material from brain extracts of two patients with FTLD-TDP, which was previously reported to induce FTLD-TDP pathology in a mouse model[35]. The sarkosyl-insoluble material was able to seed SegA monomer (Supplementary Fig. 1g), indicating that in these FTLD-TDP brain extracts, TDP-43 contains a well-folded SegA region that can serve as a template for seeded aggregation, thereby supporting the existence of the dagger-shaped fold in these extracts. In contrast, we found that the same brain extracts cannot seed SegB A315E monomer (Supplementary Fig. 1g), suggesting that the R-shaped fold may not exist in these extracts. This lack of seeding may mean that the R-shaped fold is specific for patients bearing the TDP-43 A315E mutation. Alternatively, the R-shaped fold may not exist in this particular patient with FTLD but may exist in other TDP-43 diseases or disease subtypes such as ALS, given that the A315E mutation was discovered in the context of ALS[36].

We thus propose a one-to-one correspondence between polymorph and disease subtype. More specifically, we speculate that the difference between SegA-sym and SegA-asym are so subtle that they may be associated with the same diseases, whereas the differences between the dagger- and R-shaped folds are substantial enough to perhaps be associated with different diseases. This hypothesis is supported by: (1) insoluble TDP-43 extracts from different subtypes of FTLD have distinct morphologies and biochemical properties[37];

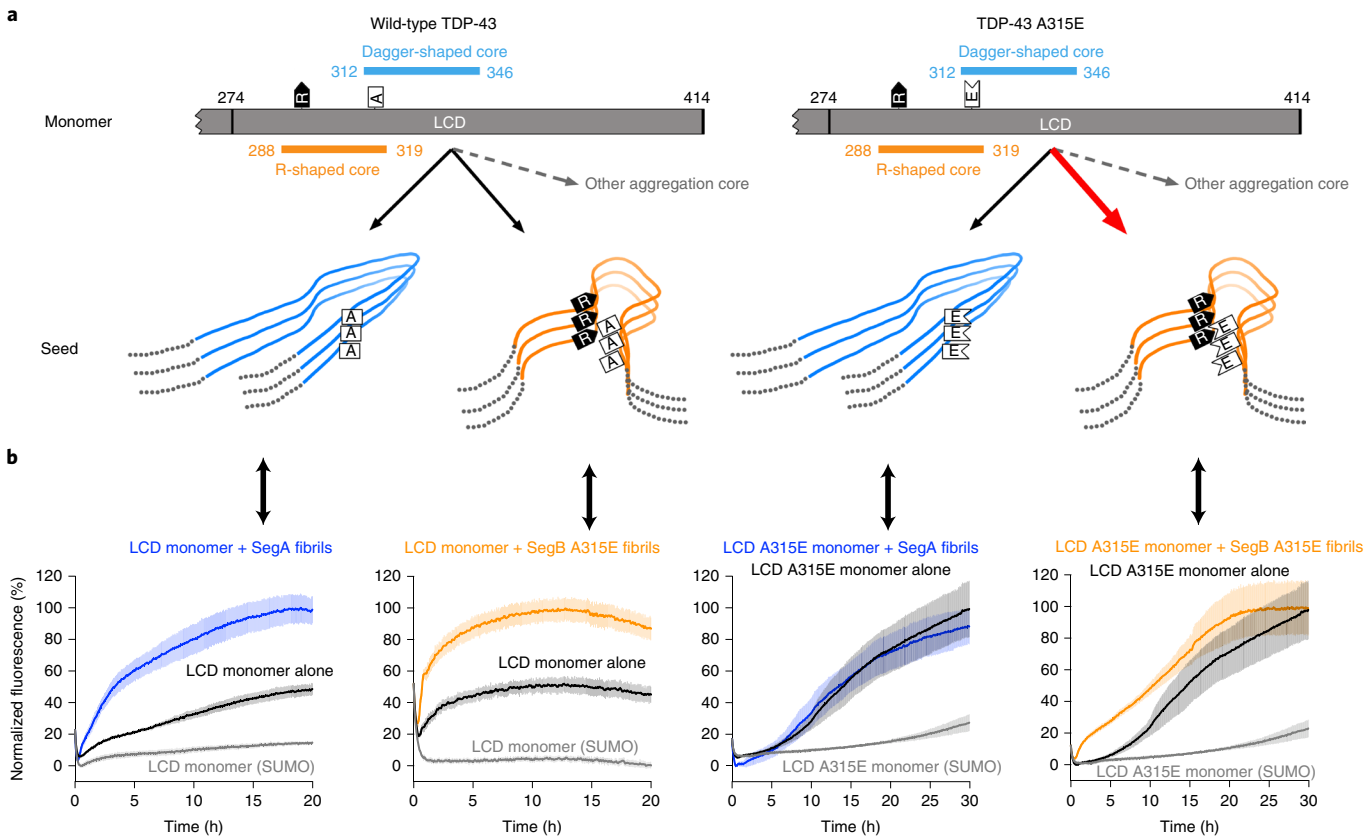

Fig. 4 | Speculative model of TDP-43 amyloid aggregation based on fibril structures reported here. a, Left: monomeric TDP-43 can form amyloid fibrils with either dagger-shaped or R-shaped cores (or perhaps other cores yet to be identified). Right: the ALS hereditary A315E mutation accelerates the R-shaped core through electrostatic interaction of E315 with R293. **b**, Experiments seeding TDP-43 fibril formation support the model in **a**. Both SegA and SegB A315E fibrils seed LCD monomer (far left and middle left). In contrast, only SegB A315E fibrils seed LCD A315E monomer, and SegA fibrils minimally seed LCD A315E monomer (far right and middle right). Data are shown as mean ± s.d., $n = 4$ independent experiments.

and (2) fibrils of two peptides whose sequences closely match the dagger-shaped fold and the R-shaped fold (Supplementary Fig. 9c) seed cell-expressed TDP-43 into distinct aggregates[33].

Discussion

Our finding of polymorphism of TDP-43 fibrils adds TDP-43 to the cohort of other polymorph-forming amyloid proteins[2,18–20] and raises the question of why polymorphism is common in amyloid fibrils but not in globular proteins. We suggest that the polymorphism observed in irreversible amyloid fibrils arises from a lack of evolutionary pressure to fold into a particular structure that performs an adaptive function. In contrast, each globular protein and functional aggregate has evolved to fold into a single structure with lower free energy than any other structure that its sequence can form. That is, pathogenic amyloid fibrils lack survival advantage and thus can adopt multiple conformations that represent different local energy minima in the protein folding landscape. However, a particular polymorph may give rise to a particular disease[38], perhaps nucleated by a mutation such as TDP-43 A315E or a particular cellular environment, as suggested for alpha-synuclein[39]. Polymorph-specific diseases are consistent with results on tau, where multiple patients with the same tauopathy all are found to have the same fibril polymorphs, and patients with different tauopathies have different fibril polymorphs[19,20,40].

Our structure of SegB A315E, the first reported cryo-EM fibril structure containing a hereditary mutation to our knowledge, offers a molecular mechanism in terms of seeding for cell-to-cell spreading of pathology through the brain[40]. Our SegB A315E structure indicates that A315E facilitates TDP-43 aggregation through electrostatic attraction with Arg293 and suggests A315T (if the threonine is phosphorylated as speculated) can function in a similar way. Wild-type TDP-43 monomer can form either the dagger-shaped or R-shaped fold (or possibly other folds), and both folds can act as seeds to recruit additional monomers into the fibril (Fig. 4a). In A315E, the interlayer interaction motif of Arg293–Glu315 provides free positive and negative charges on both ends of any R-shaped fibril that consists of at least two layers (Fig. 2h), and these free charges can attract additional monomers through long-range electrostatic interactions. Thus, the seeding potency of the R-shaped fold with the A315E mutation may exceed that of other folds. Our seeding experiments support this model by showing that SegB A315E fibrils are more effective in seeding TDP-LCD A315E monomer than SegA fibrils, as discussed below (Fig. 4b).

The observation that both SegA and SegB A315E fibrils can seed LCD monomer (Fig. 4b) indicates that the LCD can adopt both the dagger- and R-shaped folds when seeded and suggests roughly equal seeding ability of both dagger- and R-shaped folds. Additionally, we found that SegA fibrils barely seed LCD A315E monomer (Fig. 4b) whereas SegB A315E fibrils can seed LCD A315E monomer (Fig. 4b). We do not think these results arise from the incompatibility of the dagger-shaped fold with the A315E mutation, because Ala315 in the dagger-shaped fold faces the solvent so that the A315E mutation would result in an allowable solvent-facing glutamate (Supplementary Fig. 9d). Instead, as the results in Fig. 4b indicate, the seeding ability of the R-shaped fold is much higher than the dagger-shaped fold when seeding A315E monomer. In this case, the

observation that SegA fibrils barely seed LCD A315E monomer can be explained by the enhanced primary nucleation and self-seeding of LCD A315E monomer via the Arg293–Glu315 salt bridge, so that the self-seeded aggregation overwhelms the seeding of SegA fibrils. Taken together, these seeding experiments (Fig. 4b) support our hypothesis that the salt bridge introduced by A315E accelerates the aggregation of the R-shaped fibrils.

Additional mechanisms proposed for hereditary mutations to impart pathology include the shift of TDP-43 from a reversible to an irreversible assembly[41,42]. Although we have shown that both dagger- and R-shaped folds form irreversible fibrils, and others have shown that the C-terminal domain can form helical assemblies in liquid droplets[42], under certain conditions, the dagger- and R-shaped folds may also participate in reversible aggregation. Energetic analysis suggests this may be possible for the R-shaped fold. The outer two chains in the SegB A315E structure differs noticeably from the inner two chains, having a lower stabilization energy (0.79 kcal/mol per residue), close to that of the FUS structure (0.66 kcal/mol per residue), which undergoes reversible aggregation, compared with that the inner chain (0.94 kcal/mol per residue, Table 2). We speculate that the structural and energetic differences between the outer and inner chains are perhaps due to the flexibility of the R-shaped fold, owing to its high glycine content and relatively small hydrophobic core. In humans lacking the A315E mutation, the absence of the Arg293–Glu315 salt bridge would eliminate the electrostatic attraction that helps to fix the R shape, perhaps allowing the molecule to partially unfold to a more open U shape. This conformational change may further compromise the stability of the R-shaped fold by promoting the disassembly of the four-protofilament bundle, given the observation that the symmetric interface of the R-shaped fold is relatively weak (Fig. 2g), and formation of the asymmetric interface requires the closed conformation of the inner R-shaped folds. Therefore, the transition from reversible to irreversible assemblies may occur through a U–R switch, in which a more open and less bundled U-shape fold converts to a more compact and more bundled R shape. This U–R switch is possible for both wild-type and A315E, although perhaps the wild-type sequence would have a higher transition state energy, owing to the loss of the Arg293–Glu315 interaction. That is, we speculate that the A315E mutation could impose a switch from a reversible to an irreversible assembly.

We note that our energetic analysis relied on the structure of one reversible fibril and for which we have no experimental evidence regarding the role of the R-shaped polymorph in reversible TDP-43 aggregation; therefore, further research identifying structures of reversible fibrils and interrogating the role of the R shape in TDP-43 reversible aggregation is needed.

Our hypotheses proposed in the preceding four paragraphs are only two of numerous possibilities for mutation-enhanced toxicity in TDP-43 proteinopathies and may not apply to hereditary mutations other than A315E. We observed that many hereditary mutations would have a neutral or even deleterious effect on the dagger- and R-shaped folds (Supplementary Fig. 9d), consistent with the idea that there are other observed mechanisms for mutation-enhanced pathology, such as toxic gain-of-function RNA splicing activity[43]. Additionally, these mutations may influence the formation of other amyloid cores.

Our four near-atomic-resolution structures of TDP-43 amyloid fibrils establish that: (1) TDP-43 is capable of forming multiple fibrillar structural polymorphs; (2) two sequence segments of TDP-43 can form distinct stable amyloid cores, one with dagger-shaped folds and one with R-shaped folds; (3) the R293–E315 salt bridge in the R-shaped fold provides a plausible explanation of enhanced TDP-43 pathology by the ALS-related hereditary mutation A315E (and possibly A315Tp); and (4) energetic analysis highlights the structural features of amyloid fibrils that may lead to both reversible and irreversible aggregation.

Online content

Any methods, additional references, Nature Research reporting summaries, source data, statements of code and data availability and associated accession codes are available at https://doi.org/10.1038/s41594-019-0248-4.

Received: 18 April 2019; Accepted: 10 May 2019;
Published online: 24 June 2019

References

1. Anfinsen, C. B. Principles that govern the folding of protein chains. *Science* **181**, 223–230 (1973).
2. Li, B. et al. Cryo-EM of full-length α-synuclein reveals fibril polymorphs with a common structural kernel. *Nat. Commun.* **9**, 3609 (2018).
3. Zhang, W. et al. Heparin-induced tau filaments are polymorphic and differ from those in Alzheimer's and Pick's disease. *eLife* **8**, e43584 (2019).
4. Neumann, M. et al. Ubiquitinated TDP-43 in frontotemporal lobar degeneration and amyotrophic lateral sclerosis. *Science* **314**, 130–133 (2006).
5. Hasegawa, M. et al. Phosphorylated TDP-43 in frontotemporal lobar degeneration and amyotrophic lateral sclerosis. *Ann. Neurol.* **64**, 60–70 (2008).
6. Irwin, D. J. et al. Frontotemporal lobar degeneration: defining phenotypic diversity through personalized medicine. *Acta Neuropathol.* **129**, 469–491 (2015).
7. Amador-Ortiz, C. et al. TDP-43 immunoreactivity in hippocampal sclerosis and Alzheimer's disease. *Ann. Neurol.* **61**, 435–445 (2007).
8. Nakashima-Yasuda, H. et al. Co-morbidity of TDP-43 proteinopathy in Lewy body related diseases. *Acta Neuropathol.* **114**, 221–229 (2007).
9. Schwab, C., Arai, T., Hasegawa, M., Yu, S. & McGeer, P. L. Colocalization of transactivation-responsive DNA-binding protein 43 and huntingtin in inclusions of Huntington disease. *J. Neuropathol. Exp. Neurol.* **67**, 1159–1165 (2008).
10. Salajegheh, M. et al. Sarcoplasmic redistribution of nuclear TDP-43 in inclusion body myositis. *Muscle Nerve* **40**, 19–31 (2009).
11. Nelson, P. T. et al. Limbic-predominant age-related TDP-43 encephalopathy (LATE): consensus working group report. *Brain J. Neurol.* https://doi.org/10.1093/brain/awz099 (2019). .
12. Buratti, E. & Baralle, F. E. The multiple roles of TDP-43 in pre-mRNA processing and gene expression regulation. *RNA Biol.* **7**, 420–429 (2010).
13. Lee, E. B., Lee, V. M.-Y. & Trojanowski, J. Q. Gains or losses: molecular mechanisms of TDP43-mediated neurodegeneration. *Nat. Rev. Neurosci.* **13**, 38–50 (2011).
14. Iguchi, Y. et al. TDP-43 depletion induces neuronal cell damage through dysregulation of Rho family GTPases. *J. Biol. Chem.* **284**, 22059–22066 (2009).
15. Kraemer, B. C. et al. Loss of murine TDP-43 disrupts motor function and plays an essential role in embryogenesis. *Acta Neuropathol.* **119**, 409–419 (2010).
16. Wang, J. et al. Cell-autonomous requirement of TDP-43, an ALS/FTD signature protein, for oligodendrocyte survival and myelination. *Proc. Natl Acad. Sci.* **115**, E10941–E10950 (2018).
17. Tycko, R. Molecular structure of aggregated amyloid-β: insights from solid-state nuclear magnetic resonance. *Cold Spring Harb. Perspect. Med.* **6**, a024083 (2016).
18. Gremer, L. et al. Fibril structure of amyloid-β(1–42) by cryo–electron microscopy. *Science* **358**, 116–119 (2017).
19. Fitzpatrick, A. W. P. et al. Cryo-EM structures of tau filaments from Alzheimer's disease. *Nature* **547**, 185–190 (2017).
20. Falcon, B. et al. Structures of filaments from Pick's disease reveal a novel tau protein fold. *Nature* **561**, 137–140 (2018).
21. Iadanza, M. G. et al. The structure of a β 2 -microglobulin fibril suggests a molecular basis for its amyloid polymorphism. *Nat. Commun.* **9**, 4517 (2018).
22. Guenther, E. L. et al. Atomic structures of TDP-43 LCD segments and insights into reversible or pathogenic aggregation. *Nat. Struct. Mol. Biol.* **25**, 463–471 (2018).
23. Guenther, E. L. et al. Atomic-level evidence for packing and positional amyloid polymorphism by segment from TDP-43 RRM2. *Nat. Struct. Mol. Biol.* **25**, 311–319 (2018).
24. Igaz, L. M. et al. Expression of TDP-43 C-terminal fragments in vitro recapitulates pathological features of TDP-43 proteinopathies. *J. Biol. Chem.* **284**, 8516–8524 (2009).
25. Pesiridis, G. S., Lee, V. M.-Y. & Trojanowski, J. Q. Mutations in TDP-43 link glycine-rich domain functions to amyotrophic lateral sclerosis. *Hum. Mol. Genet.* **18**, R156–R162 (2009).
26. Kato, M. & McKnight, S. L. A solid-state conceptualization of information transfer from gene to message to protein. *Annu. Rev. Biochem.* **87**, 351–390 (2018).
27. Hughes, M. P. et al. Atomic structures of low-complexity protein segments reveal kinked β sheets that assemble networks. *Science* **359**, 698–701 (2018).
28. Jiang, L.-L. et al. Structural transformation of the amyloidogenic core region of TDP-43 protein initiates its aggregation and cytoplasmic inclusion. *J. Biol. Chem.* **288**, 19614–19624 (2013).

29. Guo, W. et al. An ALS-associated mutation affecting TDP-43 enhances protein aggregation, fibril formation and neurotoxicity. *Nat. Struct. Mol. Biol.* **18**, 822–830 (2011).
30. Lim, L., Wei, Y., Lu, Y. & Song, J. ALS-causing mutations significantly perturb the self-assembly and interaction with nucleic acid of the intrinsically disordered prion-like domain of TDP-43. *PLoS Biol.* **14**, e1002338 (2016).
31. Wegorzewska, I., Bell, S., Cairns, N. J., Miller, T. M. & Baloh, R. H. TDP-43 mutant transgenic mice develop features of ALS and frontotemporal lobar degeneration. *Proc. Natl Acad. Sci.* **106**, 18809–18814 (2009).
32. Xu, M. et al. Characterization of β-domains in C-terminal fragments of TDP-43 by scanning tunneling microscopy. *J. Struct. Biol.* **181**, 11–16 (2013).
33. Shimonaka, S., Nonaka, T., Suzuki, G., Hisanaga, S. & Hasegawa, M. Templated Aggregation of TAR DNA-binding Protein of 43 kDa (TDP-43) by Seeding with TDP-43 Peptide Fibrils. *J. Biol. Chem.* **291**, 8896–8907 (2016).
34. Murray, D. T. et al. Structure of FUS protein fibrils and its relevance to self-assembly and phase separation of low-complexity domains. *Cell* **171**, 615–627.e16 (2017).
35. Porta, S. et al. Patient-derived frontotemporal lobar degeneration brain extracts induce formation and spreading of TDP-43 pathology in vivo. *Nat. Commun.* **9**, 4220 (2018).
36. Fujita, Y., Ikeda, M., Yanagisawa, T., Senoo, Y. & Okamoto, K. Different clinical and neuropathologic phenotypes of familial ALS with A315E TARDBP mutation. *Neurology* **77**, 1427–1431 (2011).
37. Laferrière, F. et al. TDP-43 extracted from frontotemporal lobar degeneration subject brains displays distinct aggregate assemblies and neurotoxic effects reflecting disease progression rates. *Nat. Neurosci.* **22**, 65 (2019).
38. Clavaguera, F. et al. Brain homogenates from human tauopathies induce tau inclusions in mouse brain. *Proc. Natl Acad. Sci. USA* **110**, 9535–9540 (2013).
39. Peng, C. et al. Cellular milieu imparts distinct pathological α-synuclein strains in α-synucleinopathies. *Nature* **557**, 558 (2018).
40. Falcon, B. et al. Tau filaments from multiple cases of sporadic and inherited Alzheimer's disease adopt a common fold. *Acta Neuropathol* **136**, 699–708 (2018).
41. Ramaswami, M., Taylor, J. P. & Parker, R. Altered ribostasis: RNA-protein granules in degenerative disorders. *Cell* **154**, 727–736 (2013).
42. Conicella, A. E., Zerze, G. H., Mittal, J. & Fawzi, N. L. ALS mutations disrupt phase separation mediated by -helical structure in the TDP-43 low complexity C-terminal domain. *Structure* **24**, 1537–1549 (2016).
43. Fratta, P. et al. Mice with endogenous TDP-43 mutations exhibit gain of splicing function and characteristics of amyotrophic lateral sclerosis. *EMBO J.* **37**, e98684 (2018).

Acknowledgements

We thank H. Zhou for use of Electron Imaging Center for Nanomachines (EICN) resources. We acknowledge the use of instruments at the EICN supported by NIH (1S10RR23057 and IS10OD018111), NSF (DBI-1338135) and CNSI at UCLA. The authors acknowledge NIH AG 054022, NIH AG061847, and DOE DE-FC02-02ER63421 for support. D.R.B. was supported by the National Science Foundation Graduate Research Fellowship Program.

Author contributions

Q.C. and D.R.B. designed experiments and performed data analysis. Q.C. expressed and purified constructs and performed biochemical experiments. Q.C. and D.R.B. prepared cryo-EM samples and performed cryo-EM data collection and processing. P.G. assisted in cryo-EM data collection and processing. M.R.S. performed solvation energy calculation. All authors analyzed the results and wrote the manuscript. D.S.E. supervised and guided the project.

Competing interests

D.S.E. is an advisor and equity shareholder in ADRx, Inc.

Additional information

Supplementary information is available for this paper at https://doi.org/10.1038/s41594-019-0248-4.

Reprints and permissions information is available at www.nature.com/reprints.

Correspondence and requests for materials should be addressed to D.S.E.

Peer review information: Inês Chen was the primary editor on this article and managed its editorial process and peer review, in collaboration with the rest of the editorial team.

Publisher's note: Springer Nature remains neutral with regard to jurisdictional claims in published maps and institutional affiliations.

Methods

Construct design. Construct design of TDP-43 segments follows the same strategy as reported previously[22]. In addition to TDP-CTF (208–414) and TDP-LCD (274–414) reported in our previous study[22], constructs used in this study include full-length TDP-43 (residues 1–414), SegA (311–360), SegB (286–331, wild type or with A315E mutation) and SegAB (286–360). All TDP-43 fragments were conjugated by inserting the cDNA into a pET28a vector containing an amino terminus conjugation of SUMO protein. The SUMO protein was used to increase solubility and prevent aggregation during expression and purification. The $(His)_6$-tag on the amino terminus of the SUMO protein was used for Ni-column purification. The expression sequences of each TDP-43 fragment are shown in Supplementary Table 1.

Protein purification and SUMO-tag cleavage. Protein purification follows the same protocol reported previously[22]. Briefly, all SUMO-tagged proteins were expressed in the *Escherichia coli* BL21 (DE3) strain. LB media with 50 μg/ml kanamycin was used for cell culture. After bacterial cells were cultured at 37 °C to an OD_{600} of 0.6–0.8, 1 mM isopropyl β-D-1-thiogalactopyranoside (IPTG) was added for protein expression, and the cells were further cultured at 25 °C for 3 h. Cells were harvested and resuspended in 20 mM Tris-HCl, pH 8.0, 500 mM NaCl, 20 mM imidazole and 10% (v/v) glycerol, supplemented with 1% (v/v) halt protease inhibitor single-use cocktail (Thermo Scientific), and sonicated (3 s on/3 s of cycle, 10 min) and centrifuged (24,000*g* for 20 min) to get cell lysate. The cell lysate was mixed with homemade NucA nuclease (5000 U per liter of cell culture) and filtered before loading onto a HisTrap HP column (GE healthcare) for purification. The HisTrap column was pre-equilibrated with 20 mM Tris-HCl, pH 8.0, 500 mM NaCl and 20 mM imidazole, and the sample was washed with 20 mM Tris-HCl, pH 8.0, 500 mM NaCl and 200 mM imidazole and eluted with 20 mM Tris-HCl, pH 8.0, 500 mM NaCl and 500 mM imidazole. Eluted protein was concentrated using Amicon Ultra-15 centrifugal filters (Millipore) and stored at −80 °C for future use.

To form fibrils of the TDP-43 fragments, the SUMO-tag of each fragment was removed before aggregation. SUMO-tagged protein was mixed with 100:1 (weight basis) with homemade ULP1 protease and incubated for 1 h. When analyzed via SDS-PAGE, samples mixed with ULP1 showed bands of intact SUMO-tagged protein at 0 h; after 1 h of cleavage, the gel showed bands of free SUMO and TDP-43 fragments, as exemplified by SegA and SegB A315E cleavage shown in Supplementary Fig. 1a.

Fibril preparation and optimization. SUMO-tag removed proteins were used for fibril preparation. For all TDP-43 fragments, the starting fibril preparation conditions are the same. Protein was diluted to 50 μM concentration with 20 mM Tris-HCl, pH 8.0, 150 mM NaCl and 10 μM DTT and filtered using 0.1 μm Ultrafree-MC-VV centrifugal filters (Millipore), then incubated at 37 °C with shaking for 3 d. The morphology of each sample was checked by negative-stain transmission EM.

To achieve the necessary fibril concentration and distribution for cryo-EM structure determination, the fibril growth condition was optimized for each sample. The optimization included determining the appropriate concentration of proteins (final values ranging from 3 μM to 100 μM monomer concentration), incubating the solution without shaking (incubation temperature, 4 °C, 25 °C or 37 °C; incubation time, overnight to more than 2 weeks; Tris or phosphate buffer; salt concentration, 50 mM to 500 mM NaCl) and seeding with preformed fibrils. After optimization of all TDP-43 fragments, SegA and SegB A315E were found to have the best fibril morphology, distribution, and concentration and were therefore selected for cryo-EM structure determination. The optimized fibril morphology of each fragment is shown in Supplementary Fig. 1b.

The optimized fibril growth condition for SegA was 50 μM protein concentration, incubation in 20 mM Tris-HCl, pH 7.4, 500 mM NaCl, 10 μM DTT at 37 °C with 3 d of shaking. Two-percent (molar ratio, monomer equivalent) preformed SegA fibrils were added as seeds. After shaking, SegA fibrils were collected via centrifugation at 9,000*g* for 5 min, washed twice and resuspended to the starting volume with the same buffer as described above but using 150 mM NaCl instead of 500 mM NaCl. Fibrils in resuspension buffer were further incubated without shaking for 3 d at room temperature. Before cryo-EM sample preparation, SegA fibrils were again collected via centrifugation and resuspended with 150 mM NaCl buffer at 5% volume of that of the previous incubation (20× concentrating), and the concentrated solution was heated to 75 °C for 30 min with a PCR machine. The final heating step was necessary to de-clump SegA fibrils and optimize fibril distribution.

The optimized fibril growth condition for SegB A315E was 50 μM initial protein concentration and incubation in 20 mM Tris-HCl, pH 8.0, 150 mM NaCl, 10 μM DTT at 37 °C without shaking. Two-percent (molar ratio, monomer equivalent) preformed SegB A315E fibrils were added as seeds. After incubation, SegB A315E fibrils were collected via centrifugation at 9,000*g* for 5 min and washed twice with the same incubation buffer at 5% volume of that of the previous incubation (20× concentrating), and the concentrated solution was used for cryo-EM sample preparation.

Negative-stain transmission electron microscopy. Negative-stain transmission EM samples were prepared by applying 5 μl of fibril solution to glow-discharged 400 mesh carbon-coated formvar support films mounted on copper grids (Ted Pella, Inc.) and incubating on the grid for 2 min. The samples were then blotted off and the grids were stained with 3 μl of 2% uranyl acetate for 1 min. The grids were washed with an additional 3 μl of 2% uranyl acetate and allowed to dry for 1 min. Each grid was imaged using a T12 (FEI) electron microscope.

Cryo-EM data collection and processing. Two microliters of fibril solution was applied to a glow-discharged Quantifoil 1.2/1.3 electron microscope grid and plunge frozen into liquid ethane using a Vitrobot Mark IV (FEI). Data were collected on a Titan Krios (FEI) microscope equipped with a Gatan Quantum LS/K2 Summit direct electron detection camera (operated with 300 kV acceleration voltage and slit width of 20 eV). Super-resolution movies were collected on a Gatan K2 Summit direct electron detector, with a nominal physical pixel size of 1.07 Å/pixel (0.535 Å/pixel in super-resolution movie frames) with a dose per frame of ~1.1 $e^-/Å^2$. A total of 40 frames with a frame rate of 5 Hz were taken for each movie resulting in a final dose of ~44 $e^-/Å^2$ per image. Automated data collection was driven by the Leginon automation software package[44].

Micrographs containing crystalline ice were used to estimate the anisotropic magnification distortion using mag_distortion_estimate[45]. CTF estimation was performed using CTFFIND 4.1.8 on movie stacks with a grouping of three frames and correction for anisotropic magnification distortion[46]. Unblur[47] was used to correct beam-induced motion with dose weighting and anisotropic magnification correction, resulting in a physical pixel size of 1.06 Å/pixel and 1.064 Å/pixel for the SegB and SegA data sets, respectively.

All particle picking was performed manually with SegB A315E data set fibrils picked as a group, and SegA data set fibrils were picked separately in groups of slow twister and fast twisters using EMAN2 *e2helixboxer.py*[48] (we could not discriminate between SegA-sym and SegA-asym by eye due to their similar crossover distances and morphology; therefore, SegA-sym and SegA-asym particles were later separated by 2D classification and 3D classification). Particles were extracted in RELION using the 90% overlap scheme into 288 pixel boxes for SegA and 320 pixel boxes for SegB A315E. Classification, helical reconstruction, and 3D refinement were used in RELION as described previously[23,49,50]. In general, we performed 2D classifications with higher tau_fudge (ranging from values of 4 to 12) to identify and select, for future 3D classification, particles contributing to 2D classes showing β-strand separation along the helical axis. We performed 3D classification with the estimated helical parameters from each structure and an elongated Gaussian blob as an initial model to generate starting reconstructions. We ran additional 3D classifications using the preliminary reconstructions from the previous step to select for particles contributing to homogenous classes (stable helicity and separation of β-strands in the x−y plane). Typically, we performed Class3D jobs with $K=3$ and manual control of the tau_fudge factor and healpix to reach a resolution of ~5–6 Å to select for particles that contributed to the highest-resolution class for each structure. For the SegB and SegA-slow reconstructions, we performed high-resolution gold-standard refinement as described previously[50]. For SegA-sym and SegA-asym, perhaps owing to low particle numbers, Refine3D seemed unable to adequately regulate working resolution to refine with high enough resolution factors to allow SegA-sym and SegA-asym reconstructions to refine past 4.8 Å, and gold-standard refinement did not result in near-atomic-resolution maps. Therefore, we employed a 'suboptimal' manual refinement protocol using all particles against a single reference map, as described previously[2,23]. Final overall resolution estimates were calculated from the corrected Fourier shell correlations of two half-maps, using high-resolution phase randomization as implemented in RELION PostProcess to account for effects of a soft-edged solvent mask and to monitor possible overfitting for the SegA-sym and SegA-asym manual refinements[51]. For the SegB and SegA-slow gold-standard refinements, we report the 0.143 FSC resolution cutoff; however, for the SegA-sym and SegA-asym suboptimal refinements, we report the 0.5 FSC resolution cutoff (the particles contributing to the final map were split *a posteriori* into even and odd micrographs to prevent particles from the same fibril contributing to different reconstructions and two half-maps were reconstructed using the fully refined center and orientation parameters)[51]. In all cases except the SegA-slow, the default value of 30% was used for the *helical_z_percentage* during 3D classification and refinement. Because the crossover distance of the SegA-slow varied from 1,200–2,000 Å, we used 10% for the *helical_z_percentage* to minimize the blurring, owing to the variable twist, as described previously[19]. Reconstructions were compared against the reference-free 2D class averages to confirm their validity. Additionally, de novo model building also confirmed the validity of the 3D reconstructions.

Specific determination of helical symmetry for all structures was performed as follows. For SegA-sym, SegA-asym, and SegB A315E, we estimated the crossover distances using a combination of manual inspection of the micrographs and inspection of 2D class averages using larger particle box sizes to capture the entire crossover distance (box sizes from 432 to 1,024 pixels were tested). In the case of the SegA-sym and the SegB A315E, the mirror symmetry axis parallel to the helical axis in the 2D class averages indicated either a two-start helix symmetry with a rise of 2.4 Å or a C_n rotational symmetry. Computed diffraction patterns from the 2D class averages indicated that there was no meridional reflection at 4.8 Å, indicating the lack of C_n rotational symmetry. Therefore, for both of these species, a helical rise of 2.4 Å was assumed, and the helical twist was calculated from the previously

estimated crossover distance. Convergence to a stable helicity and high-resolution refinement to near-atomic resolution allowing de novo model building confirmed the helical symmetry. For SegA-slow, the entire crossover distance could not be captured by the 1,024-pixel box size, so the crossover distance was estimated from a combination of manual inspection of micrographs and a 'stitched'-together fibril using the 2D classes from the 288 box size (Supplementary Fig. 3f). Class averages, as well as the computed diffraction pattern from the 'stitched' fibril, confirm the presence of a meridional reflection at 4.8 Å, indicating C_n rotational symmetry. Therefore, we assumed a helical rise of 4.8 Å, and we calculated the helical twist from the previously estimated crossover distance. High-resolution refinement to near-atomic resolution allowed de novo model building, confirming the helical symmetry. Additionally, reconstructions with a helical rise of 2.4 Å did not show clear side chain density, and projections of the reconstruction did not match the 2D class averages (Supplementary Fig. 3e). For SegA-asym, the crossover distance was estimated from a combination of inspection of the micrographs, and 2D class averages with larger box sizes. Owing to the lack of apparent two-fold symmetry in the 2D class averages, we assumed a helical rise of 4.8 Å and calculated the helical twist from the measured crossover distances. Refinement to near-atomic resolution shows that the two SegA-asym monomers within each asymmetric unit are not identical, thus confirming the lack of two-fold symmetry.

Atomic model building. We sharpened the refined maps using phenix.auto_sharpen[52] at the resolution cutoff indicated by half-map FSC and subsequently built atomic models into the refined maps with COOT[53]. For the three SegA polymorphs, we built the model of SegA-slow first, owing to its high resolution (3.3 Å). The density map of SegA-slow clearly shows a cyclic main chain with the amino and carboxy termini at the center of the fibril. The initial model was built with both N−C orientations, and only the orientation shown in the current model fit all the side chain densities. The conservation of the dagger fold in the maps of SegA-sym and SegA-asym, especially the signature ^{334}WGMMGML^{340} motif, allowed us to rigid-body fit the model of SegA-slow into SegA-sym and SegA-asym maps. After rigid-body fitting, we manually inspected and adjusted each residue.

After building atomic models for the main chain of SegA polymorphs, we observed extra density peripheral to the dagger-shaped fold around Gln331 of SegA-slow and Met323 of both SegA-asym and SegA-slow (Fig. 1c,d). We believe this density arises from unstable interactions (because of either weak binding or binding of a mixture of different residues) of other protomers with the core protofilaments. We could not build a definitive model because of the ambiguity of the side chain densities; however, we built a hypothetical model into the density near Gln331 of SegA-slow based on the speculation that this density represents part of the continuous dimer interface found in SegA-sym and SegA-asym.

During model building of SegA-slow, we found that the model that fully recapitulates the registration of SegA-sym was not favorable due to the steric clash at Leu340 and unexplained side chain density at Gly338 (Supplementary Fig. 6c). Therefore, we built the model with a registration that has a two-residue offset compared with SegA-sym. We believe that this registration shift is allowed by the similarity of nearby residues (Gln331 from the dagger fold flanked by Ser342 and Gln344 from the short chain, compared with Gln331 flanked by Gln344 and Gln346), and is caused by the lack of the hydrophobic anchor formed by Met336 and Leu340 (Supplementary Fig. 6d). A similar registration shift was observed in previously reported crystal structures of steric zippers and was termed 'registration polymorphism'[54]. The extra densities near Met323 in SegA-asym and SegA-slow could represent an additional dimer interface that protects Ala321, Met323 and Ala325 from the solvent, but without unambiguous side chain density, we could not build in any models for these densities.

The model building of SegB A315E was initiated by the inspection of the density map near the homodimer interface on the neck of the inner chain R-shaped fold. The side chain density and nearby environment indicates the atomic model of this region should feature four or five small side chain residues flanked by a big side chain residue on each side, and the only motif in the SegB A315E sequence that matches this criterion is ^{293}RGGGAGL^{299}, with only one orientation feasible considering the length of density at each side of this motif. With the model of ^{293}RGGGAGL^{299} built, the rest of the model was built by adding the residues one by one. All side chains fit the density unambiguously. The observation that Glu315 forms a salt bridge with Arg293 further supports this model. After we built the inner R-shaped fold, we speculated that the outer R-shaped fold was not a continuation of the same chain as the inner R-shaped fold, because there were not enough residues in the sequence to accommodate the outer R-shaped fold. Therefore, the model of the outer R-shaped fold was built de novo, similarly to the inner-R-shaped fold.

For all structures, after we built the initial model, we used in-house scripts to generate a five-layer model using the helical symmetry of the refined map and used phenix.real_space_refine for model refinement[55]. After several rounds of refinement, we adjusted the orientation of the main chain oxygen and nitrogen to facilitate main chain hydrogen bonding within the β-sheet, and we applied these main chain hydrogen bond restraints for further real-space refinement. As the last step, the rotamer of each serine, glutamine and asparagine residue was manually inspected to ensure the energy-favorable hydrogen binding. The final model was validated using MolProbity[56].

The G304W model of SegB A315E shown in Supplementary Fig. 9b was generated by manually changing Gly304 residues of the one-layer SegB A315E model (four glycine residues in four chains) to tryptophan in COOT, and we generated a five-layer mutated model using the same script as that for the original SegB A315E model. We refined this five-layer mutated model with phenix.real_space_refine using, the same density map we used to refine the original model. The refined model shows no Ramachandran angles and rotamer outliers and no significant clashes. The statistics of SegB A315E G304W model are shown in Supplementary Table 3, and the coordinates are listed as Supplementary Data Set 1.

Energetic calculation. The stabilization energy is an adaptation of the solvation free energy described previously[57], in which the energy was calculated as the sum of products of the area buried of each atom and its corresponding atomic solvation parameter (ASP). ASPs were taken from our previous work[57]. Area buried was calculated as the difference in solvent accessible surface area (SASA) of the reference state (unfolded state) and the SASA of the folded state. The reference state was measured absent all other atoms in the structure but the residue "i" and main chain atoms of residue i−1 and i+1. The SASA of the folded state was measured for each atom in the context of all amyloid fibril atoms. Fibril coordinates were extended by symmetry by three to five chains on either side of the reported molecule, to ensure the energetic calculations were representative of the majority of molecules in a fibril, rather than a fibril end. To account for energetic stabilization of main chain hydrogen bonds, the ASP for backbone N/O elements was reassigned from −9 to 0 if they participated in a hydrogen bond. Similarly, if an asparagine or glutamine side chain participated in a polar ladder (two hydrogen bonds per amide) and was shielded from solvent ($SASA_{folded} < 5$ Å^2), the ASPs of the side chain N and O elements were reassigned from −9 to 0. Lastly, the ASP of ionizable atoms (for example, aspartate, glutamine, lysine, histidine, arginine, N-terminal amine, or C-terminal carboxylate) were assigned the charged value (−37/−38), unless the atoms participated in a buried ion pair, defined as a pair of complementary ionizable atoms within a 4.2 Å distance of each other, each with $SASA_{folded}$ < 40 Å^2). In that case, the ASP of the ion pair was reassigned to −9. In the energy diagrams, a single color is assigned to each residue, rather than each atom. The color corresponds to the sum of solvation free energy values of each of the atoms in the residue. The energy reported for FUS in Table 2 is the average over 20 NMR models. The standard deviation is 1.8 kcal/mol.

Thermostability assays of TDP-43 and FUS fibrils. To validate the energetic calculations and test the stability of TDP-43 segment fibrils experimentally, preformed TDP-43 segment fibrils were heated at 75 °C for 30 min in a PCR machine, and the existence of the fibrils were checked by negative-stain EM. All fibrils were heated in 20 mM Tris, pH 7.4, 150 mM NaCl, 10 μM DTT at 50 μM monomer-equivalent concentration.

FUS protein was purified, and FUS fibrils were formed the same way as previously reported[27]. FUS protein was expressed using pHis-parallel-mCherry-1FUS214 plasmid that contained the LCD of FUS (1–214) conjugated to mCherry. Purification was done with an Ni column and size exclusion column. The hydrogel of FUS was formed by incubating purified mCherry-FUS at 4 °C for 2 weeks at a concentration of 1 M. After hydrogel formation, a scrape of hydrogel was mixed with 20 mM Tris, pH 7.4, 150 mM NaCl, 10 μM DTT to approximately 20× of its original volume (~50 μM monomer concentration). The mixture was allocated to three PCR tubes, one without heat and two heated at 60 °C and 75 °C for 30 min, respectively. All three samples were checked for fibrils via negative-stain EM. The sample without heat contained abundant fibrils on the EM grid and the sample with heat contains no visible fibrils anywhere on the EM grid.

ThT assays. Protein was diluted to 12 μM in 20 mM Tris-HCl, pH 7.4, 500 mM NaCl, 10 μM DTT, 30 μM ThT, and filtered using 0.1 μm Ultrafree-MC-VV centrifugal filters (Millipore). Filtered solution was mixed with or without 100:1 (weight basis) ULP1, with or without 5% (molar ratio, monomer equivalent) preformed fibril seeds (or 1% v/v for brain extract seeds), and was pipetted into a polybase black 384-well plate with optical bottom (Thermo Scientific) and incubated at 37 °C without shaking. ThT fluorescence was measured with excitation and emission wavelength of 440 and 480 nm, respectively, using FLUOstar Omega plate reader (BMG LABTECH). The aggregation curves were averaged from four independent measured replicates and error bars show s.d. of replicate measurements. Fibril seeds were sonicated (1 s on/1 s off cycle, 3 min) before use to increase the seeding ability.

The brain extracted materials were a generous gift from the lab of V. Lee. Brain extract #1 was from a patient diagnosed as FTLD-TDP, and brain extract #2 was from a patient diagnosed as FTLD-TDP-GRN. Both brain extracts were extracted from the frontal cortex, and estimated TDP-43 concentration was ~500 ng/ml (measured by ELISA assays), and estimated total protein concentration was 2.5 mg/ml for brain extract #1 and 4 mg/ml for brain extract #2 (measured using bicinchoninic acid assays).

The samples mixed with preformed fibril seeds had an additional ThT background reading because of the seeds. To better compare the curves of samples

with and without seeding and estimate the ThT signal change that represented the formation of seeded fibrils, we removed the background by subtracting the value of the first reading from each curve. To normalize the different ranges of fluorescence readings observed from each experiments (probably due to the different fluorescence gain settings of the plate reader), we normalized the readings to make the minimum mean value in each panel 0% and the maximum mean value in each panel 100%.

TDP-CTF aggregation assays. The aggregation assays of pathological fragments of TDP-43 (TDP-CTF) were performed mostly as previously reported[22]. The SUMO-TDP-CTF wild type and mutants were diluted into 0.2 mg/ml with 20 mM Tris-HCl, pH 8.0, 150 mM NaCl, 10 μM DTT and filtered by 0.1 μm Ultrafree-MC-VV centrifugal filters (Millipore). To simplify the experiment, we did not remove the SUMO-tag by ULP1 protease, because we found that wild-type TDP-CTF aggregates after overnight incubation even with the protection of SUMO. Filtered samples were incubated at 4 °C overnight and separated into supernatant and pellet fractions by centrifugation at 18,000*g* for 3 min at 4 °C. The pellet was resuspended with the same buffer and volume, and both supernatant and pellet were mixed with 3:1 (v/v) of NuPAGE LDS sample buffer (Invitrogen) and heated to 100 °C for 10 min. The pre-incubation samples were directly mixed with sample buffer and heated to 100 °C for 10 min as above. All samples were separated by NuPAGE 4–12% Bis-Tris gels (Invitrogen) and stained with Coomassie blue. TDP-CTF A324W that was previously shown to reduce TDP-CTF aggregation[22] was also tested in this study as a control to confirm that we got similar results with and without ULP1 cleavage.

Reporting Summary. Further information on research design is available in the Nature Research Reporting Summary linked to this article.

Data availability

All structural data have been deposited into the Worldwide Protein Data Bank (wwPDB) and the Electron Microscopy Data Bank (EMDB) with the following accession codes: SegA-sym (PDB 6N37, EMD-9339), SegA-asym (PDB 6N3B, EMD-9350), SegA-slow (PDB 6N3A, EMID-9349), SegB A315E (PDB 6N3C, EMD-0334). Coordinates for the structural model of SegB A315E G304W are in Supplementary Data Set 1. All other data are available from the authors upon reasonable request.

Code availability

Custom software used for solvation energy calculation and for generating multilayer models is available from the authors upon reasonable request.

References

44. Suloway, C. et al. Automated molecular microscopy: the new Leginon system. *J. Struct. Biol.* **151**, 41–60 (2005).
45. Grant, T. & Grigorieff, N. Automatic estimation and correction of anisotropic magnification distortion in electron microscopes. *J. Struct. Biol.* **192**, 204–208 (2015).
46. Rohou, A. & Grigorieff, N. CTFFIND4: Fast and accurate defocus estimation from electron micrographs. *J. Struct. Biol.* **192**, 216–221 (2015).
47. Grant, T. & Grigorieff, N. Measuring the optimal exposure for single particle cryo-EM using a 2.6 Å reconstruction of rotavirus VP6. *eLife* **4**, e06980 (2015).
48. Tang, G. et al. EMAN2: an extensible image processing suite for electron microscopy. *J. Struct. Biol.* **157**, 38–46 (2007).
49. He, S. & Scheres, S. H. W. Helical reconstruction in RELION. *J. Struct. Biol.* **198**, 163–176 (2017).
50. Scheres, S. H. W. RELION: Implementation of a Bayesian approach to cryo-EM structure determination. *J. Struct. Biol.* **180**, 519–530 (2012).
51. Chen, S. et al. High-resolution noise substitution to measure overfitting and validate resolution in 3D structure determination by single particle electron cryomicroscopy. *Ultramicroscopy* **135**, 24–35 (2013).
52. Terwilliger, T. C., Sobolev, O. V., Afonine, P. V. & Adams, P. D. Automated map sharpening by maximization of detail and connectivity. *Acta Crystallogr. Sect. Struct. Biol.* **74**, 545–559 (2018).
53. Emsley, P., Lohkamp, B., Scott, W. G. & Cowtan, K. Features and development of Coot. *Acta Crystallogr. D Biol. Crystallogr.* **66**, 486–501 (2010).
54. Wiltzius, J. J. W. et al. Molecular mechanisms for protein-encoded inheritance. *Nat. Struct. Mol. Biol.* **16**, 973–978 (2009).
55. Afonine, P. V. et al. Real-space refinement in PHENIX for cryo-EM and crystallography. *Acta Crystallogr. Sect. Struct. Biol.* **74**, 531–544 (2018).
56. Chen, V. B. et al. MolProbity: all-atom structure validation for macromolecular crystallography. *Acta Crystallogr. D Biol. Crystallogr.* **66**, 12–21 (2010).
57. Eisenberg, D., Wesson, M. & Yamashita, M. Interpretation of protein folding and binding with atomic solvation parameters. *Chemica Script* **29A**, 217–222(1989).

nature research

Corresponding author(s): David S. Eisenberg

Last updated by author(s): May 9, 2019

Reporting Summary

Nature Research wishes to improve the reproducibility of the work that we publish. This form provides structure for consistency and transparency in reporting. For further information on Nature Research policies, see Authors & Referees and the Editorial Policy Checklist.

Statistics

For all statistical analyses, confirm that the following items are present in the figure legend, table legend, main text, or Methods section.

n/a	Confirmed
☐	☒ The exact sample size (*n*) for each experimental group/condition, given as a discrete number and unit of measurement
☐	☒ A statement on whether measurements were taken from distinct samples or whether the same sample was measured repeatedly
☒	☐ The statistical test(s) used AND whether they are one- or two-sided *Only common tests should be described solely by name; describe more complex techniques in the Methods section.*
☒	☐ A description of all covariates tested
☒	☐ A description of any assumptions or corrections, such as tests of normality and adjustment for multiple comparisons
☒	☐ A full description of the statistical parameters including central tendency (e.g. means) or other basic estimates (e.g. regression coefficient) AND variation (e.g. standard deviation) or associated estimates of uncertainty (e.g. confidence intervals)
☒	☐ For null hypothesis testing, the test statistic (e.g. *F*, *t*, *r*) with confidence intervals, effect sizes, degrees of freedom and *P* value noted *Give P values as exact values whenever suitable.*
☒	☐ For Bayesian analysis, information on the choice of priors and Markov chain Monte Carlo settings
☒	☐ For hierarchical and complex designs, identification of the appropriate level for tests and full reporting of outcomes
☒	☐ Estimates of effect sizes (e.g. Cohen's *d*, Pearson's *r*), indicating how they were calculated

Our web collection on statistics for biologists contains articles on many of the points above.

Software and code

Policy information about availability of computer code

Data collection	Automated Cryo-EM data collection was driven by the Leginon automation software package (v3.0)
Data analysis	Anisotropic magnification distortion was estimated by software mag_distortion_estimate (version 0.0.0). CTF estimation was performed using CTFFIND (version 4.1.8). Beam-induced motion was corrected by Unblur (version 1.0.0). Particle picking was performed using EMAN2 (version 2.2) e2helixboxer.py. Classification, helical reconstruction, and 3D refinement were performed in RELION (version 2.1.0). Refined maps were sharpened using phenix.auto_sharpen (version 1.13-2998). Atomic models were built in COOT (version 0.8.9.1). Model refinement was performed with phenix.real_space_refine (version 1.13-2998). Structures were presented using PyMOL (version 2.2.0). ThT curves were generated using GraphPad Prism (version 7.0c). Energetic calculations were performed using custom written software, and the software is available to anyone inquiring.

For manuscripts utilizing custom algorithms or software that are central to the research but not yet described in published literature, software must be made available to editors/reviewers. We strongly encourage code deposition in a community repository (e.g. GitHub). See the Nature Research guidelines for submitting code & software for further information.

Data

Policy information about availability of data

All manuscripts must include a data availability statement. This statement should provide the following information, where applicable:

- Accession codes, unique identifiers, or web links for publicly available datasets
- A list of figures that have associated raw data
- A description of any restrictions on data availability

All structural data have been deposited into the Worldwide Protein Data Bank (wwPDB) and the Electron Microscopy Data Bank (EMDB) with the following accession codes: SegA-sym (PDB 6N37, EMD-9339), SegA-asym (PDB 6N3B, EMD-9350), SegA-slow (PDB 6N3A, EMID-9349), SegB A315E (PDB 6N3C, EMD-0334). All other data are available from the authors upon reasonable request.

Field-specific reporting

Please select the one below that is the best fit for your research. If you are not sure, read the appropriate sections before making your selection.

☒ Life sciences ☐ Behavioural & social sciences ☐ Ecological, evolutionary & environmental sciences

For a reference copy of the document with all sections, see nature.com/documents/nr-reporting-summary-flat.pdf

Life sciences study design

All studies must disclose on these points even when the disclosure is negative.

Sample size	Sample sizes for ThT assays were 4 and are generally considered as sufficient for plate-reader based experiments.
Data exclusions	No data were excluded from the results.
Replication	All attempts at replication were successful.
Randomization	Randomization is not relevant to our study. No research animal, human research participants or clinical studies are involved in our study.
Blinding	Blinding was not relevant to our study. No subjective analysis were required.

Reporting for specific materials, systems and methods

We require information from authors about some types of materials, experimental systems and methods used in many studies. Here, indicate whether each material, system or method listed is relevant to your study. If you are not sure if a list item applies to your research, read the appropriate section before selecting a response.

Materials & experimental systems

n/a	Involved in the study
☒	☐ Antibodies
☒	☐ Eukaryotic cell lines
☒	☐ Palaeontology
☒	☐ Animals and other organisms
☒	☐ Human research participants
☒	☐ Clinical data

Methods

n/a	Involved in the study
☒	☐ ChIP-seq
☒	☐ Flow cytometry
☒	☐ MRI-based neuroimaging